Circumplanetary disk ices
II. Composition

Oberg, N.; Cazaux, S.; Kamp, I.; Bründl, T. M.; Thi, W. F.; Immerzeel, C.

DOI
10.1051/0004-6361/202245592

Publication date
2023

Document Version
Final published version

Published in
Astronomy and Astrophysics

A&A 672, A142 (2023)
https://doi.org/10.1051/0004-6361/202245592

Astronomy & Astrophysics

Circumplanetary disk ices

II. Composition

N. Oberg[1,2], S. Cazaux[2,3], I. Kamp[1], T.-M. Bründl[2,3], W. F. Thi[4], and C. Immerzeel[2]

[1] Kapteyn Astronomical Institute, University of Groningen, PO Box 800, 9700 AV Groningen, The Netherlands
e-mail: oberg@astro.rug.nl
[2] Faculty of Aerospace Engineering, Delft University of Technology, Kluyverweg 1, 2629 HS Delft, The Netherlands
[3] University of Leiden, PO Box 9513, 2300 RA, Leiden, The Netherlands
[4] Max-Planck-Institut für extraterrestrische Physik, Giessenbachstrasse 1, 85748 Garching, Germany

Received 30 November 2022 / Accepted 6 February 2023

ABSTRACT

Context. The subsurface oceans of icy satellites are among the most compelling among the potentially habitable environments in our Solar System. The question of whether a liquid subsurface layer can be maintained over geological timescales depends on its chemical composition. The composition of icy satellites is linked to that of the circumplanetary disk (CPD) in which they form. The CPD accretes material from the surrounding circumstellar disk in the vicinity of the planet, however, the degree of chemical inheritance is unclear.
Aims. We aim to investigate the composition of ices in chemically reset or inherited circumplanetary disks to inform interior modeling and the interpretation of in situ measurements of icy solar system satellites, with an emphasis on the Galilean moon system.
Methods. We used the radiation-thermochemical code ProDiMo to produce circumplanetary disk models and then extract the ice composition from time-dependent chemistry, incorporating gas-phase and grain-surface reactions.
Results. The initial sublimation of ices during accretion may result in a CO_2-rich ice composition due to efficient OH formation at high gas densities. In the case of a Jovian CPD, the sublimation of accreted ices results in a CO_2 iceline between the present-day orbits of Ganymede and Callisto. Sublimated ammonia ice is destroyed by background radiation while drifting towards the CPD midplane. Liberated nitrogen becomes locked in N_2 due to efficient self-shielding, leaving ices depleted of ammonia. A significant ammonia ice component remains only when ices are inherited from the circumstellar disk.
Conclusions. The observed composition of the Galilean moons is consistent with the sublimation of ices during accretion onto the CPD. In this scenario, the Galilean moon ices are nitrogen-poor and CO_2 on Callisto is endogenous and primordial. The ice composition is significantly altered after an initial reset of accreted circumstellar ice. The chemical history of the Galilean moons stands in contrast to the Saturnian system, where the composition of the moons corresponds more closely with the directly inherited circumstellar disk material.

Key words. planets and satellites: formation – planets and satellites: composition – astrochemistry – methods: numerical – protoplanetary disks

1. Introduction

The search for habitable worlds beyond the solar system has historically focused on planets in the so-called "habitable zone", where surface conditions theoretically support the presence of liquid water (Hart 1979). In the Solar System, however, icy satellites and minor bodies outside of the classical habitable zone are the most common type of worlds that are known to host oceans of liquid water (Hussmann et al. 2006; Nimmo & Pappalardo 2016). Evidence strongly supports the presence of a subsurface ocean on the Galilean satellites Europa and Ganymede, as well as (to a lesser extent) Callisto (Carr et al. 1998; Khurana et al. 1998; Kivelson et al. 2002; Sohl et al. 2002; Saur et al. 2015). The resonant configuration of the satellites prevents a damping of the orbital eccentricities, producing levels of tidal heating capable of sustaining subsurface oceans over geological timescales (Peale & Lee 2002; Hussmann & Spohn 2004; Showman et al. 1997). Whether or not a given level of tidal heating produces subsurface melt depends in part on the composition of the satellite ices. The proposed abundant impurities include NH_3, CH_4, CO, and CO_2, along with salts $MgSO_4$ and NaCl (Kargel 1992; Mousis & Alibert 2006). The liquidus temperature of co-deposited ice mixtures can be depressed by the presence of NH_3 (Choukroun & Grasset 2010; Sohl et al. 2010) or methanol (CH_3OH; Deschamps et al. 2010; Dougherty et al. 2018), as well as salts to a lesser extent. Hence, the composition of the volatile reservoir from which icy satellites form is of direct relevance to the presence of a subsurface ocean, their geothermal and physical evolution (Hammond et al. 2018), the interpretation of in situ geophysical measurements (Vance et al. 2018), and the eventual atmospheric composition by outgassing or impact dissociation (Sekine et al. 2014; Glein 2015).

In particular, ammonia is important to the interior state and evolution of icy bodies. The presence of NH_3 in the form of dihydrate can drive differentiation of rock and ice (Desch et al. 2009). Ammonia in a pure H_2O-NH_3 eutectic system produces a freezing point depression of ~100 K (Kargel 1992; Grasset et al. 2000; Leliwa-Kopystyński et al. 2002). Ammonia can also reduce the density of melt with implications for buoyancy and cryovolcanism (Croft et al. 1988), while increasing viscosity and reducing

the efficiency of convection (Grasset et al. 2000). Ammonia has been detected in the plumes of Enceladus (Waite et al. 2009) but not on the surface of the Galilean moons. Tentative evidence for a subsurface ocean on Callisto would be bolstered by the presence of an ammonia component of 1–5% (Kirk & Stevenson 1987; Showman & Malhotra 1999; Spohn & Schubert 2003).

In the "gas-starved" circumplanetary disk (CPD) paradigm, moon formation occurs in a relatively low-mass, cool disk that must accumulate solids to form giant moons over time (Canup & Ward 2002, 2006; Batygin & Morbidelli 2020). Infalling material from the surrounding circumstellar disk may be shock-heated in the process of accretion onto the CPD (Szulágyi 2017; Szulágyi & Mordasini 2017; Aoyama et al. 2018), with increasing shock temperature for increasing planetary mass. If the shock heating chemically resets infalling gas or ices, new ice formation must occur within the CPD to produce the icy satellites we see today. The resulting composition of the satellite ices may then depart substantially from those in the planetary feeding zone.

Prior works modeling equilibrium condensation chemistry in a Jovian CPD suggest that in the event of an initial vaporization of ices, the "mostly inefficient" gas-phase reactions lead to ratios of CO_2:CO:CH_4 and N_2:NH_3 that are not substantially different from those in the feeding zone of Jupiter (Mousis & Alibert 2006; Mousis et al. 2006). However, it has long been recognized that grain-surface chemistry plays a critical role in the formation of many common molecules under interstellar conditions (Hasegawa et al. 1992; van Dishoeck & Blake 1998; Cazaux & Tielens 2002; Caselli et al. 2004; Garrod et al. 2006; Ruaud et al. 2015; Wakelam et al. 2017). The use of a more comprehensive modeling approach including grain-surface and photochemistry to revisit the formation of ices in CPDs is thus motivated. We aim to investigate the composition of ices that form in a chemically reset CPD with viscous timescale 10^3–10^4 yr, where infalling ices are sublimated and gas is atomized by shock-heating. These results will be contrasted with a partial reset in which only ices are sublimated during accretion and with a full chemical inheritance scenario in which the composition of the circumstellar disk gas and ice is preserved. We intend to link observations of solar system icy satellites with modern chemical disk models to lay the foundation for our understanding of how icy moons are built up from material in the CPD.

2. Methods

We used the radiation-thermochemical disk modeling code ProDiMo[1] to model gas and dust chemistry and physics in disks (Woitke et al. 2009, 2016; Kamp et al. 2010, 2017; Thi et al. 2011, 2020). The gas-grain chemistry is solved self-consistently with the 2D radiative transfer and heating and cooling balance using a rate equation-based approach. Most reaction rates are selected from the UMIST2012 database (McElroy et al. 2013) and three-body collider reactions are adopted from the UMIST2006 rate file (Woodall et al. 2007), as they were not included in the 2012 release. In the following sections we review the implementation of the grain surface chemistry (Sect. 2.1), extensions to our standard chemical network (Sect. 2.2), and properties of the CPD model (Sect. 2.3).

2.1. Grain surface chemistry

ProDiMo includes a rate-equation based, statistical two-phase approach to gas and dust grain surface chemistry that is largely based on the work of Hasegawa et al. (1992). Gas-phase atoms and molecules can become weakly adsorbed to grain surface physisorption sites. Physisorbed species diffuse in a random-walk process "hopping" from one physisorption site to another (Barlow & Silk 1976). Diffusion occurs thermally if there is sufficient energy to overcome a diffusion barrier or can otherwise occur by tunneling. The surface diffusion rate is the sum of the thermal, tunneling, and cosmic-ray induced diffusion rates. The rate of thermal diffusion of species, i, is:

$$R_i^{\rm diff,th} = \nu_{0,i} Q_i^{\rm diff}(a_i^{\rm diff}, E_i^{\rm diff}) e^{\Delta E_{ij}/k_{\rm B}T_{\rm d}} / n b_{\rm site}\ {\rm s}^{-1}, \quad (1)$$

where $k_{\rm B}$ is the Boltzmann constant, $T_{\rm d}$ is the dust temperature, and the frequency term, $\nu_{0,\rm i}$, describing characteristic lattice vibration is:

$$\upsilon_{0,i} = \sqrt{\frac{2N_{\rm surf}E_i^{\rm b}}{\pi^2 m_i}}, \quad (2)$$

$N_{\rm surf}$ is the surface density of adsorption sites 1.5×10^{15} cm^{-2}. The number of adsorption sites per monolayer on a grain of radius a is $nb_{\rm site} = 4\pi N_{\rm surf} a^2$. Also, $E_{\rm i}^{\rm b}$ is the binding energy and m_i is the mass of the species. We use a tunneling-corrected form of the Arrhenius equation, Bell's formula, $Q_i^{\rm diff}$, to determine the surface diffusion tunneling rate (Bell 1980):

$$Q_i^{\rm diff} = \frac{\beta e^{-\alpha} - \alpha e^{-\beta}}{\beta - \alpha}, \quad (3)$$

where

$$\alpha = E_i^{\rm diff}/k_{\rm B}T_{\rm d} \quad (4)$$

and

$$\beta = \frac{4\pi a_i^{\rm diff}}{h}\sqrt{2m_i E_i^{\rm diff}}. \quad (5)$$

Here, $E_i^{\rm diff}$ is the diffusion activation energy, $a_i^{\rm diff}$ is the diffusion activation barrier width, and h is the Planck constant. ΔE_{ij} is the difference in binding energy between two adsorption sites, i and j. We have $\Delta E_{ij} = 0$ if $E_i^b \le E_j^b$, thus, for a random hop between two physisorption sites, $\Delta E = 0$. The cosmic-ray induced diffusion rate $R_i^{\rm diff,CR}$ is adopted from (Hasegawa & Herbst 1993; Reboussin et al. 2014):

$$R_i^{\rm diff,CR} = f(70\,{\rm K}) R_i^{\rm diff,th}(70\,{\rm K}) \frac{\zeta_{\rm CR}}{5\times10^{-17}}{\rm s}^{-1}, \quad (6)$$

where $\zeta_{\rm CR}$ is the cosmic ray ionization rate and $f(70\,{\rm K}) = 3.16\times10^{-19}$ is the duty-cycle of the grain at 70 K. The total diffusion rate, $R_i^{\rm diff}$, is then the sum of the thermal and cosmic-ray induced diffusion rates.

Species that are physisorbed to a grain surface can react directly with species coming from the gas-phase (Eley-Rideal) or with other physisorbed species (Langmuir–Hinshelwood). Reaction products can remain on the grain surface or chemically desorb into the gas-phase. Reactions between physisorbed species follow the prescription of Hasegawa et al. (1992). The reaction rate coefficients between two surface-adsorbed species is the probability of a reaction per encounter multiplied by the encounter rate between the two species diffusing across the surface. The encounter rate between two adsorbed species i and j hopping across the surface is then:

$$k_{ij} = \kappa_{ij}(R_i^{\rm diff} + R_j^{\rm diff})/n_d\ \ {\rm cm}^3{\rm s}^{-1}, \quad (7)$$

[1] https://prodimo.iwf.oeaw.ac.at/

where κ_{ij} is the reaction probability, $R_i^{\rm diff}$ and $R_j^{\rm diff}$ are the diffusion rates (s^{-1}) for species, i and j, and $n_{\rm d}$ is the dust grain number density (cm^{-3}). The reaction probability, κ_{ij}, takes into account the competition between association of the species and diffusion (Garrod & Pauly 2011; Bonfanti & Martinazzo 2016; Ruaud et al. 2016):

$$\kappa_{ij} = \frac{Q_{\rm Bell}(a_{ij}^r, E_i^{\rm act})}{Q_{\rm Bell}(a_{ij}^r, E_i^{\rm act}) + P_i^{\rm diff} + P_j^{\rm diff}}, \quad (8)$$

where a_{ij}^r is the reactive barrier width, $E_i^{\rm act}$ is the activation energy of the reaction barrier, and $P_i^{\rm diff} = R_i^{\rm diff}/\nu_{0,i}$.

We assume the semi-equilibrium theory in which reactions between physisorbed and gas-phase species (Eley-Rideal) is equal to the probability of the gas atom colliding with the physisorbed species multiplied by the probability of the gas-phase species having sufficient energy to overcome the reaction barrier. Impinging gas-phase species are assumed to have an energy relative to the surface species $1/2k_{\rm B}T_{\rm g} + E_i^b$, where $T_{\rm g}$ is the gas temperature and E_i^b is the binding energy. Photon and cosmic-ray induced dissociation and desorption of grain-surface species are also included. Adsorption and desorption processes are described fully in Thi et al. (2020).

2.2. Extending chemistry beyond the standard network

We developed an extended chemical network based on the "DIANA standard large" network described in Kamp et al. (2017), which contains 235 species (including 63 ices) and 12 elements + polycyclic aromatic hydrocarbons (PAHs) and is optimized for gas-phase chemistry + direct adsorption and desorption from grains. The use of grain-surface reactions necessitates the inclusion of several additional species to the DIANA standard chemical network to capture the relevant chemistry occurring at the disk midplane. These seven additional gas-phase species and six additional ices are listed in Table 1. Physisorbed atomic hydrogen and H_2 are included for their critical role in many grain-surface reactions. Hydrogenated PAH and O_2H are included for their relevance to the chemical reset scenario in which atomic H is initially very abundant. The rationale for their inclusion is discussed in the following sections. In addition, HOCO and HCOOH are more directly involved in the formation of relevant ices and their roles are discussed in Sect. 3.1.3.

Hydrogenated polyclic aromatic hydrocarbons (PAH-H). In ProDiMo, the formation rate of H_2 can be calculated in multiple ways. The standard approach is that H_2 formation proceeds via a pseudo-reaction at a rate calculated according to the analytical approach of Cazaux & Tielens (2002)m which presupposes that surface-chemisorbed H atoms play a dominant role at high temperatures (≥100 K). However, the formation of H_2 is calculated explicitly when grain-surface reactions are included in the reaction network (Thi et al. 2020). It was noted in the accompanying work that H_2 formation occurs in parallel with H_2O ice deposition on grains at the midplane when the CPD is chemically reset (Oberg et al. 2022 hereafter, Paper I). The formation of H_2O ice after the reset is rapid and a median-sized grain is coated in several (≫3) monolayers of water ice prior to the complete conversion of H to H_2. This poses a problem as the formation of H_2 via surface-chemisorbed H is considered implausible when the number of water ice monolayers exceeds a certain number (~3; Wakelam et al. 2017). We assume that the diffusion timescale of the atomic hydrogen in a water ice matrix and subsequent difficulty of H_2 escape from the grain silicate surface precludes this formation pathway in our scenario. An alternative path to form H_2 is via hydrogenated polycyclic aromatic hydrocarbons (PAH-H; Bauschlicher 1998). Experimental and theoretical works have demonstrated that H_2 can form via Eley-Rideal abstractions on neutral PAHs (Bauschlicher 1998; Rauls & Hornekær 2008; Mennella et al. 2012; Thrower et al. 2012) and cationic PAHs (Hirama et al. 2004; Cazaux et al. 2016; Boschman et al. 2012). We include in the chemical network the singly hydrogenated species PAH-H, PAH-H^+, and the physisorbed ice form PAH-H# (Thrower et al. 2009) to enable this formation path.

Table 1. Non-standard species included in the chemical network.

Gas-phase species	
O_2H	
HOCO	
HCOOH	
$HCOOH^+$	
$HCOOH_2^+$	
PAH-H	
$PAH\text{-}H^+$	
Ices	$E_{\rm ads}$ [K]
H#	$600^{(1)}$
H_2#	$430^{(2)}$
O_2H#	$3650^{(2)}$
HOCO#	$2000^{(3)}$
HCOOH#	$5000^{(4)}$
PAH-H#	$5600^{(5)}$

Notes. Adsorption energies are adopted from [(1)]Cazaux & Tielens (2002), [(2)]Garrod & Herbst (2006), [(3)]Ruaud et al. (2015), [(4)]Öberg et al. (2009) and [(5)]Thrower et al. (2009).

As a first step towards H_2 formation, the neutral or ionized PAH is hydrogenated with a small (324 K) activation barrier. The H_2 formation at the CPD midplane then proceeds primarily via

$$\text{PAH-H} + \text{H} \rightarrow \text{H}_2 + \text{PAH}, \quad (9)$$

and to a lesser extent (~1−10% of the total H_2 formation rate depending on location in the CPD), directly via the gas-phase neutral-neutral reactions:

$$\text{H} + \text{HCO} \rightarrow \text{H}_2 + \text{CO}, \quad (10)$$

$$\text{H} + \text{HNO} \rightarrow \text{H}_2 + \text{NO}. \quad (11)$$

While we do include several grain-surface reactions to form H_2 (e.g., H# + HCO# → CO# + H_2#, O# + H_2CO# → CO_2# + H_2#); in practice, these occur at a negligible rate due to the 50 K minimum dust temperature in the CPD. The resulting efficiency of H_2 formation is lower than the analytic rate of Cazaux & Tielens (2002) in part due to the low ambient temperatures (<200 K, which in combination with the activation barrier impede the process) at the optically thick midplane. The correspondingly longer time over which atomic hydrogen is present has direct consequences for the efficiency of water formation. Gas-phase H_2O can then form via the hydrogenation of OH for an extended period of time (discussed further in Paper I).

O_2H. The hydroperoxyl radical O_2H is a very reactive oxygen species that we have found to play a role in the formation

of methanol in the inner region of chemically reset CPDs. We include the gas and ice form of O_2H in the extended chemical network, with an adsorption energy of 3650 K (Garrod & Herbst 2006). The oxygen-bearing gas-phase species abundances are sensitive to the presence of O_2H at high densities. Three-body collider reactions with free atomic hydrogen and O_2 produce O_2H. This reaction has been extensively studied both theoretically (Horowitz 1985; Sellevåg et al. 2008; Morii et al. 2009) and experimentally (Kurylo 1972; Davidson et al. 1996; Hahn et al. 2004; Mertens et al. 2009) at high and low temperatures. With the inclusion of O_2H in the extended network the gas-phase O_2 reservoir at the midplane (nominally present at an abundance $\sim 10^{-4.4}$ relative to hydrogen in the standard network) is depleted and converted via OH into H_2O through the following reactions

$$O_2 + H + M \rightarrow O_2H + M, \quad (12)$$

or

$$O_2 + HCO \rightarrow O_2H + CO, \quad (13)$$

followed by

$$O_2H + H \rightarrow OH + OH, \quad (14)$$
$$OH + H \rightarrow H_2O + \text{photon}. \quad (15)$$

These reactions compete for the free H that is required to form methanol via

$$H_2CO + H \rightarrow CH_3O, \quad (16)$$
$$CH_3O + H \rightarrow CH_3OH, \quad (17)$$

and thus suppress its formation. The inclusion of O_2H in the chemical network reduces the abundance of methanol ice interior to the NH_3 iceline relative to the results of the standard chemical network by 90–99%. However, this has a negligible impact on the total disk-integrated methanol abundance.

2.3. Circumplanetary disk model

We adopted the properties of the PRODIMO circumplanetary disk model developed in Paper I. The CPD is a "gas-starved", actively fed accretion disk (Canup & Ward 2002) that is heated primarily by viscous dissipation at the midplane (D'Alessio et al. 1998; Frank et al. 2002). The parameters of the reference CPD model are listed in Table 2. The physical, radiative, and thermal properties of the CPDs are demonstrated in Paper I, namely, Figs. 3 and 4.

The disk structure in terms of radial and vertical dimension, density profile, dust-to-gas ratio, and temperature, are assumed to exist in a steady-state and are kept fixed. Following the gas-starved disk paradigm, the CPD does not instantaneously contain the solid mass required to form the Galilean satellites. The total refractory dust mass is $1.7 \times 10^{-5}\ M_\oplus$ and exists in the form of small grains (0.05–3000 μm). The dust grain size distribution is described by a smooth power-law $n \propto a^{-3.5}$. Such a disk is optically thick out to approximately ~1/3rd of the planetary Hill radius R_H, which is coincident with the theoretical limit for stable orbits (Quillen & Trilling 1998; Ayliffe & Bate 2009; Martin & Lubow 2011).

For the ice-to-rock ratio of the solids in the CPD to be consistent with the ice-to-rock ratio of the outer Galilean satellites, it was found in Paper I that the dust-to-gas ratio of the CPD may be depleted relative to the canonical 10^{-2} by a factor $\gtrsim$10–20. This depletion in dust corresponds with the rapid inwards drift and loss of grains larger than ~150 μm, which was found to occur naturally for a disk with a mass of $10^{-7}\ M_\odot$ and accretion rate $\dot{M} = 10^{-11} M_\odot\ \mathrm{yr}^{-1}$ (Paper I). Alternatively, pressure-bump trapping at the gap edge can directly prevent larger grains from accreting onto the CPD (Rice et al. 2006; Morbidelli & Nesvorny 2012; Zhu et al. 2012; Bitsch et al. 2018). For assumptions regarding the efficiency of settling, surface density power-law, and maximum grain size, it was found in Paper I that the global dust-to-gas ratio should not exceed $10^{-3.3}$ for a CPD with a mass of $10^{-7}\ M_\odot$ and accretion rate of $\dot{M} = 10^{-11}\ M_\odot\ \mathrm{yr}^{-1}$ to satisfy the constraints on Jovian icy moon bulk composition. The properties of the disk models are further justified and detailed in Paper I, where the authors explored a small grid of plausible CPD parameters.

In this work, our analysis is focused on the case of the $10^{-7}\ M_\odot$ CPD with accretion rate $\dot{M} = 10^{-11} M_\odot\ \mathrm{yr}^{-1}$, as it was most closely able to reproduce the radial ice-to-rock ratio of the Galilean satellites while being consistent with the circumstellar disk gas component expected lifetime. We contrast our results with those of the "high" viscosity, hotter CPD with $\dot{M} = 10^{-10} M_\odot \mathrm{yr}^{-1}$ and correspondingly shorter viscous timescale 10^3 yr given uncertainties in the magnitude of the disk viscosity.

Table 2. Parameters of the reference CPD model.

Parameter	Symbol	Value
Planetary mass	M_p	1.0 M_J
Planetary luminosity	L_p	$10^{-5}\ L_\odot$
Effective temperature	$T_{eff,p}$	1000 K
UV luminosity	$L_{UV,p}$	0.01 L_p (*)
Interstellar UV field	χ	3×10^3
Background temperature	T_{back}	50 K
Disk mass	M_{cpd}	$10^{-7}\ M_\odot$
Disk inner radius	$R_{in,cpd}$	0.0015 au
Exponential decay radius	$R_{in,cpd}$	0.11 au
Disk outer radius	$R_{out,cpd}$	0.34 au
Column density power ind.	ϵ	1.0
Accretion rate	$\dot{M}$	10^{-11}–$10^{-10}\ M_\odot\ \mathrm{yr}^{-1}$
Viscosity	α	$10^{-3.6}$–$10^{-2.7}$
Minimum dust size	a_{min}	0.05 μm
Maximum dust size	a_{max}	3000 μm
Dust-to-gas ratio	d/g	$10^{-3.3}$
Flaring index	β	1.15
Reference scale height	$H_{0.1au}$	0.01 au

Notes. (*)Planetary UV luminosity is expressed in multiples of the planetary luminosity, L_p.

2.3.1. Initial chemical conditions

Three different initial chemical conditions are considered. The first case is a full chemical "reset", in which ices are initially sublimated and the circumstellar gas is reverted to a purely atomic, ionized state. A chemical reset may occur if, for instance, the circumstellar material is shock-heated during accretion onto the CPD, if the gas and dust are irradiated while crossing the optically thin gap, or if material only flows into the gap from the upper optically thin surface layers of the circumstellar disk. The CPD model is initialized in this fully reset state after which it is allowed to chemically evolve over its viscous timescale t_{visc}. The viscous timescale of the disk is defined as the time over which

the majority of the gas mass is lost $t_{visc} = M_{cpd}/\dot{M}$, where $\dot{M}$ is the mass accretion rate. We assume that gas is lost to viscous radial flow either to decretion beyond the disk edge or accretion onto the planet. As the disk mass is assumed to be constant, the net inflow-outflow rate of matter is necessarily zero. Our reference CPD model has a viscous timescale of 10^4 yr with a corresponding midplane heating rate equivalent to an α-viscosity of $10^{-3.6}$. We contrast these results with a "partial reset" in which only the ices are placed back in the gas-phase. This is similar to the work of Mousis & Alibert (2006) wherein the authors consider a case in which infalling ices are initially sublimated in a warm disk which subsequently cools, although we consider a disk with a static temperature structure. Finally we consider an "inheritance" case in which the chemical composition at the circumstellar disk outer edge is used as the initial state. The abundance of the most common species for these three initial conditions can be found in Appendix B. The circumstellar disk model and the sampling of the inheritance chemistry are described in the accompanying Paper I.

2.3.2. Vertical diffusion of gas and dust

It is also necessary to consider the consequences of the gas and dust being shocked at several scale heights above the CPD midplane (Takasao et al. 2021) prior to the gas turbulently diffusing downwards into the optically thick region. The ambient conditions at ~5 pressure scale heights ($A_V = 0.01$) differ significantly from those at the midplane ($A_V = 21$) given the magnitude of the external stellar irradiation. To take into account this gradual change in ambient conditions, we incorporated an additional step necessary to prevent the sublimated ices immediately re-adsorbing to grains. We adapted the model to follow a single parcel of gas and dust that is initialized above the midplane and then settles towards the midplane at the centrifugal radius (~0.03 R_H; Machida et al. 2008). This process is labeled as step 2 in Fig.1.

In this step, we evolved the chemistry in a 0D grid-cell for a fraction of the diffusion timescale. The resulting composition of the gas and ice was extracted and used to populate a new grid-cell, in which the background conditions are updated to correspond to the downwards motion of the gas parcel. The extracted relative species abundances were simply applied to the new cell and absolute abundances were rescaled to correspond to the new grid-cell density. This process was repeated iteratively as ambient conditions (optical depth, density, and gas and dust temperature) change. As a simplification owing to significant uncertainties in the origin, magnitude, and spatial distribution of turbulence within the CPD, we simply assumed that the parcel travels at a constant rate until it reaches the midplane. The timescale of this process is ~10 yr (Paper I), although this value is still highly uncertain. Accordingly, we also considered diffusion timescales of 1, 10, and 100 yr. The final composition of the parcel at the midplane was then used to populate the CPD midplane for the final step (step 3 in Fig. 1), whereby chemical evolution proceeds up until the viscous timescale.

2.4. Likelihood of chemical reset and magnitude of shock-heating

Icy grains passing through an optically thin gap at 5 au around a Sun-like star can retain their icy mantles if swept up by the planet within ~10−100 orbital timescales (Paper I). If a (partial) chemical reset occurs, it must instead be due to either accreted material originating from a higher altitude in the circumstellar disk where ices are unstable or, otherwise, shock-heating on the CPD surface. We can estimate the shock velocity of infalling matter where it strikes the CPD and consider which of our initial chemical conditions corresponds most appropriately to the formation of the Galilean moon system. Angular momentum of infalling circumstellar gas and dust causes it to accrete onto the CPD near the so-called centrifugal radius, r_{cf} (Hayashi et al. 1985; Machida et al. 2008). The infall velocity at r_{cf} must be $\gtrsim$8−10 km s^{-1} for dust grain icy mantles to be lost due to sputtering and thermal desorption (Woitke et al. 1993; Aota et al. 2015; Tielens 2021). We approximated the infall velocity as a function of planetocentric radius by considering orbits with apoapsis of a single circumstellar disk pressure scale height at the position of Jupiter (z = 0.5 au; Paper I), with orbital eccentricities corresponding to passage through the planet equatorial plane at some distance r. The resulting infall velocities, v_{infall}, can be seen in Fig. 2 for planets of Saturnian, Jovian, and super-Jovian (10 M_J) mass. The infall velocity at r_{cf} is independent of the planetary mass, but it is instead a function of the planetary semimajor axis (for a circular orbit). The shock velocity at the centrifugal radius of Jupiter is in the regime of icy mantle loss to sputtering (Draine & McKee 1993; Tielens 2005). Hence, if the majority of grains accrete near r_{cf}, Jupiter's CPD may be best represented by the "partial reset" scenario. Conversely, no ice sublimation is expected to occur due to shock-heating in the case of Saturn. A full chemical reset is more likely to occur for a super-Jupiter at a stellocentric distance of 2–3 au from a solar-mass star.

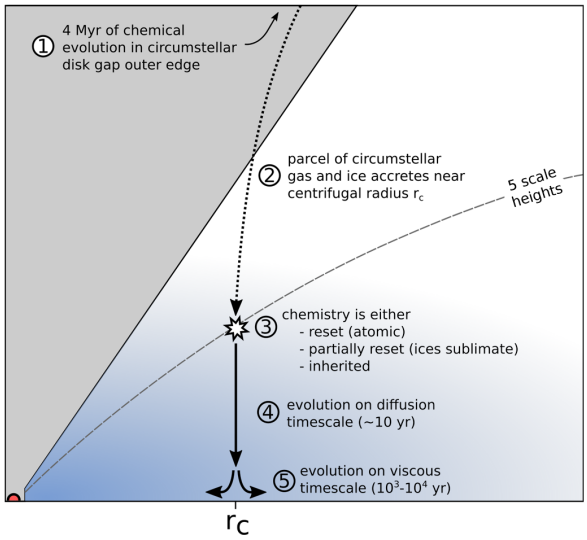

Fig. 1. Schematic illustration of the modeling process. In step 1, the chemistry in a circumstellar disk model is evolved for 4 Myr. This chemistry is extracted from the gap outer wall region and used as a starting point prior to accretion. To consider various possible accretion scenarios, the composition of the infalling material is either reset to atomic (full reset), the ices are sublimated (partial reset) or the chemistry remains unaltered (inherit). In step 2, the chemistry of a parcel of gas and ice is evolved for 10 yr as it travels towards the CPD midplane. In step 3, the chemistry is evolved at the CPD midplane for the viscous timescale of the disk.

2.5. Chemical network diagrams

Throughout this work, we make use of algorithmically generated chemical network diagrams to describe relations between atomic and molecular species, their relative abundances, formation rates, and the types of reactions that are involved. The

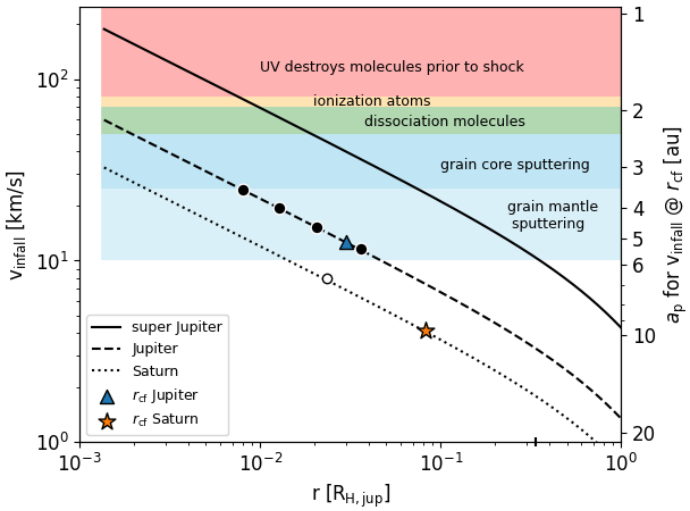

Fig. 2. Velocity of material falling onto a CPD $v_{\rm infall}$ at radius r for planets of Saturnian (dotted line), Jovian (dashed lines), and super-Jovian (10 $M_{\rm J}$, solid line) mass. The centrifugal radii $r_{\rm cf}$ of Jupiter and Saturn are indicated by the blue triangle and orange star, respectively. The radial position of the Galilean satellites is indicated by the four black circles and the radial position of Titan is indicated by the white circle. The planetary orbital radius, $a_{\rm p}$, that corresponds to the infall velocity at the centrifugal radius, $v_{\rm infall}(r_{\rm cf})$, is indicated on the right vertical axis. The shaded colored regions indicate different chemical consequences of shock-heating corresponding to a given $v_{\rm infall}$. The units on the abscissa are in multiples of the Jovian Hill radius. All calculations correspond to a solar mass star.

diagrams are generated with an implementation of the PyVis software package (itself based on the VisJS library Perrone et al. 2020). A description of how these diagrams are generated and interpreted can be found in Appendix A.

3. Results and discussion

Prior to reaching the midplane, the accreted gas and dust diffuses downwards from the optically thin surface layer of the CPD at the centrifugal radius, $r_{\rm c}$. We iteratively evolved the disk chemistry as the background conditions change during the descent. The relevant properties of the vertical slice through the circumplanetary disk during the descent to the midplane at $r_{\rm c}$ can be found in Fig. 3a. The post-shock evolution of the water ice abundance during the descent to the midplane can be found in Figs. 3b–d for the reset, partial reset, and inheritance cases, respectively. Solid lines trace the evolution of ice impurity abundances as the gas parcel moves downwards from five scale heights (left) to the midplane (right). Dashed lines trace the abundances in the case of a hotter, higher viscosity CPD with $t_{\rm visc} = 10^3$ yr. The initial pre-shock abundances of the impurities are indicated by the colored circles on the ordinate.

In the case of the reference (low-viscosity) fully or partially reset CPD, significant quantities of water ice have already formed prior to reaching the midplane. In the fully reset case, the ice is predominantly water with <0.1% impurities in the form of CH_3OH and HCOOH ice. In the partial reset case, a significant (25%) CO_2 component has formed. In the inheritance case, ices are able to survive the brief exposure to the optically thin upper layers of the disk and the CPD accretes a nitrogen-rich ice composition. In the high-viscosity ($\alpha = 10^{-3}$) CPD model, ices are not thermally stable at the centrifugal radius midplane. This can be seen in Fig. 3, where ice abundances decline immediately prior to reaching the midplane. Consequently the initial

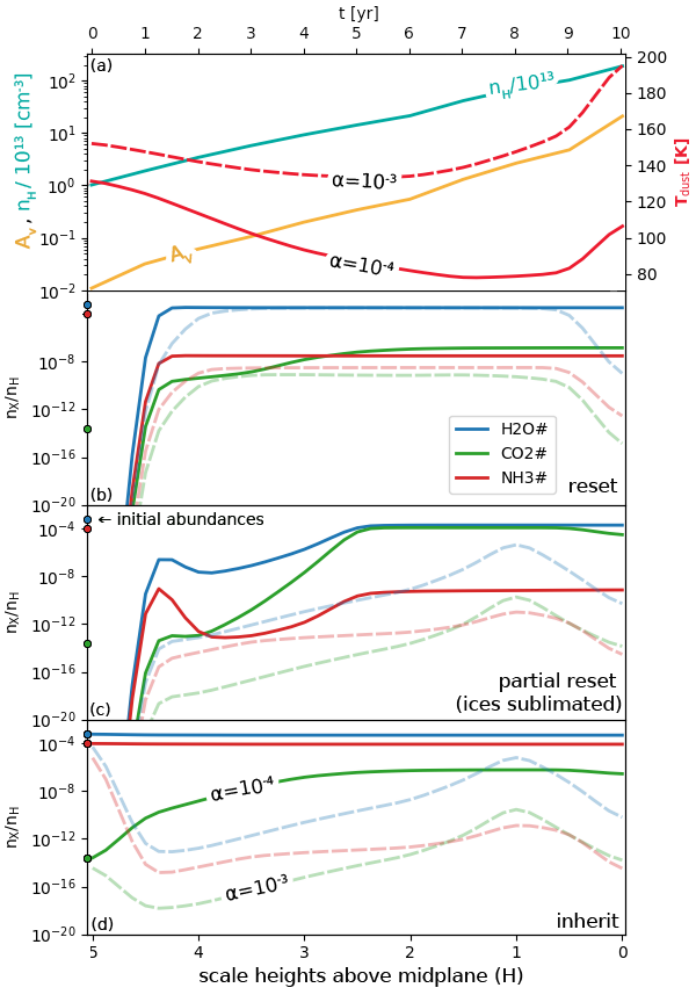

Fig. 3. (*a*) Properties of a vertical slice in the circumplanetary disk at the centrifugal radius, from five pressure scale heights (left) to the midplane (right). Evolution of the abundance of H_2O, NH_3 and CO_2 ice as the parcel of gas and dust sinks to the midplane after accretion in the reset case: (*b*) in the partial reset case (*c*) and the inheritance case (*d*). Solid lines trace the relevant properties and abundances for the low viscosity ($t_{\rm visc} = 10^4$ yr) case and the dashed line describes the high viscosity ($t_{\rm visc} = 10^3$ yr) case.

post-shock conditions of a "partial reset" and "inheritance" converge to a similar ice-free molecular gas composition by the time the gas parcel reaches the midplane.

After the step involving the accreted gas and dust being followed as it travels towards the midplane (step 4 in Fig. 1), the resulting chemical abundances are used to specify the initial conditions for the rest of the CPD as it evolves on the viscous timescale (step 5 in Fig. 1). After 10^3–10^4 yr of further evolution, we extracted the radial ice composition at the midplane from six distinct CPD models describing three initial chemical conditions (reset, partial reset, and inheritance) and two disk α-viscosities (corresponding to viscous timescales of 10^3 and 10^4 yr). An overview of the radial midplane ice composition, the disk-integrated total molecular ice composition, and the disk-integrated total elemental ice budget of the low-viscosity CPDs can be found in Fig. 4. For reference, the ice-to-rock ratio of the solids at the CPD midplane is also included in Fig. 4 (left column) as a solid white line. The settling of large grains to the midplane strongly reduces the local ice-to-rock ratio. Realistically, accreting moons may be able to capture solids drifting

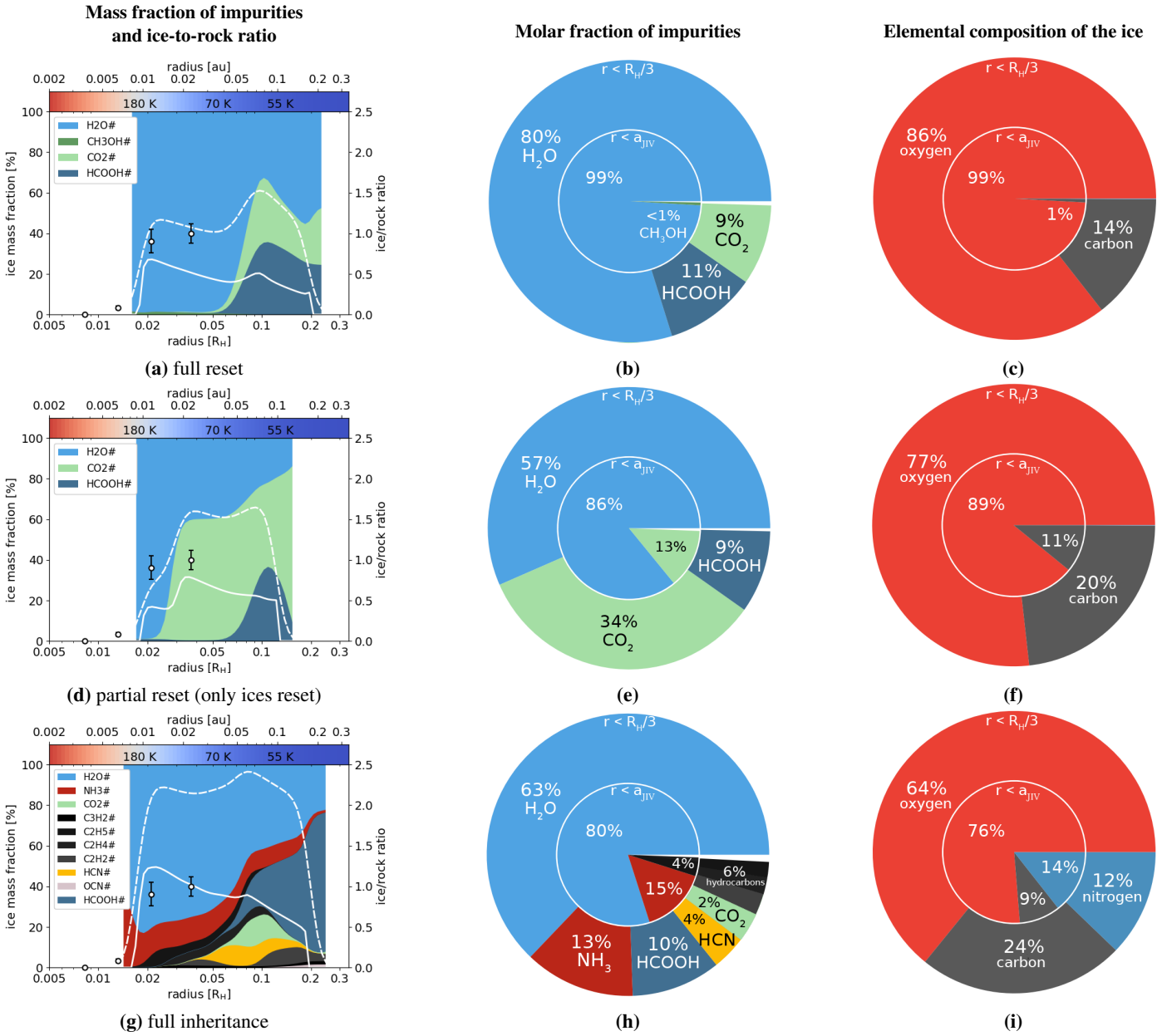

Fig. 4. Overview of the chemical composition at the CPD midplane for the "full reset" case (*top row*), for the "partial reset" case (*middle row*), and for the "full inheritance" case (*bottom row*). *Left column*: radial mass fraction of ices at the CPD midplane (filled-colored regions) where $f_{\rm ice} > 0.01$. The white lines indicate the radial ice-to-rock ratio of solids at the midplane (solid line) and integrated up to an altitude above the midplane equal to the Hill radius of Ganymede (dashed line). The estimated ice-to-rock ratio of the Galilean satellites is included (circles with error bars). *Center column*: radially integrated midplane ice composition out to $R_{\rm H}/3$ (outer ring) and within the orbit of Callisto $a_{\rm JIV}$ (inner circle). *Right column*: total disk-integrated elemental composition of the ices are shown in the same two radial zones.

at higher altitudes above the midplane within their gravitational sphere of influence. Hence, we included also the ice-to-rock ratio of solids integrated up to an altitude equal to the Hill radius of a Ganymede-mass object (dashed white line). The radial abundance profiles of NH_3, HCOOH, CO_2, and CH_3OH ices can be found in Fig. 5.

Ices at the partially or fully reset CPD midplane are found to contain significant impurities in the form of CO_2 and HCOOH, as well as, to a lesser extent, CH_3OH. The chemically inherited CPD additionally contains HCN and hydrocarbon ices which were already present at the time of accretion. Trace amounts of OCN, SO, SO_2, NH, NH_2, OH, and HNO ices can also be found, but each at <0.1−0.5% of the total ice mass. Although several of these ices have negligible absolute abundances, the fraction of their key element which has frozen out can be substantial. In particular, sulfur has frozen completely out of the gas-phase outside of the centrifugal radius in all cases. The element fraction in ice can be found in Appendix C. In the following subsections, we discuss the formation and abundance of the impurities NH_3, CO_2, HCOOH, and CH_3OH.

3.1. Partial reset (initial sublimation of ices)

It is likely that in the case of the Jupiter system, the shock velocity of matter accreting at the centrifugal radius did not lead to the full dissociation of molecules. A less extreme C-type

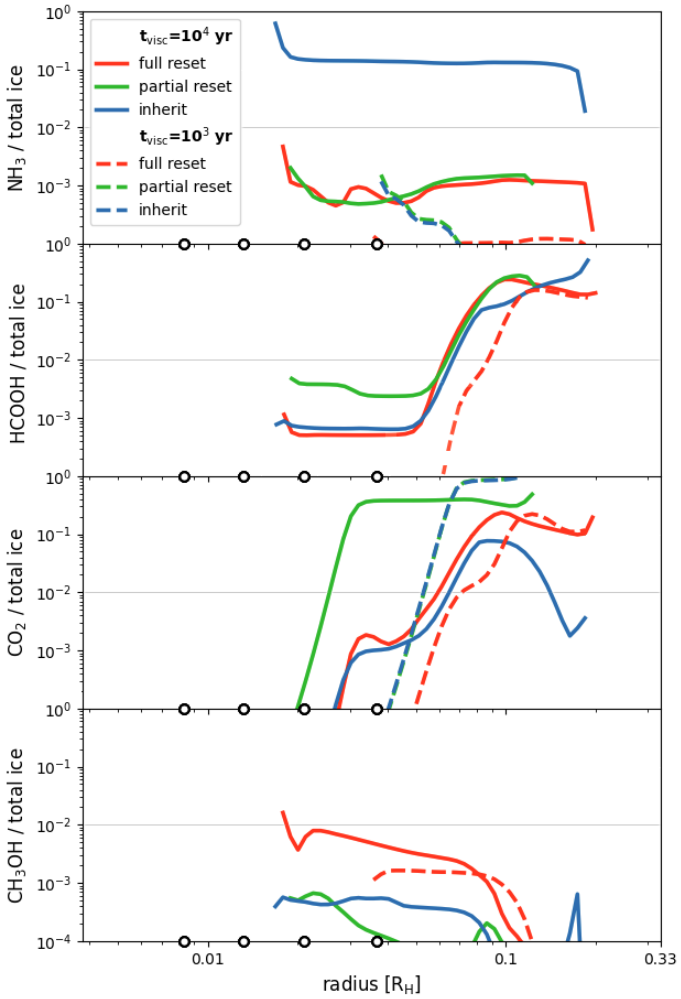

Fig. 5. Radial abundance of selected non-H_2O ices as a fraction of the total ice abundance for the low-viscosity case with $t_{visc} = 10^4$ yr (solid lines) and high-viscosity case with $t_{visc} = 10^3$ yr (dashed lines). The position of the Galilean satellites are indicated by the empty circles. A light gray horizontal line indicates a concentration of 1%.

shock-heating could simply cause icy grain mantles to desorb by sputtering, for instance. Accordingly, we focus our analysis and discussion on this case, whereby all ices are put back into their respective gas-phase counterpart.

3.1.1. Ammonia (NH_3)

Immediately after accretion onto the CPD and the sublimation of ices, hydrogen is predominantly found in the form of H_2, oxygen in H_2O, and nitrogen in NH_3 and HCN at a ratio 1:0.63. After ten years of drifting towards the midplane the gas is still H_2-dominated, but nitrogen is found primarily in N_2. After being initially sublimated a minor fraction of the NH_3 immediately re-adsorbs to the grains (see Fig. 3c), but it is not stable against photodissociation given the background UV field intensity ($\chi_{RT} > 1000$). Above 2–3 scale heights, the NH_3 ice is photodissociated on the grain surface to, for instance, NH_2# and H# or back into the gas phase as NH. Once the majority of nitrogen is locked into N_2 via NH+NH, it is stable against photodissociation due to self-shielding (Li et al. 2013), preventing the accumulation of NH_3. The photodissociation timescale of N_2 is much larger than the disk viscous timescale.

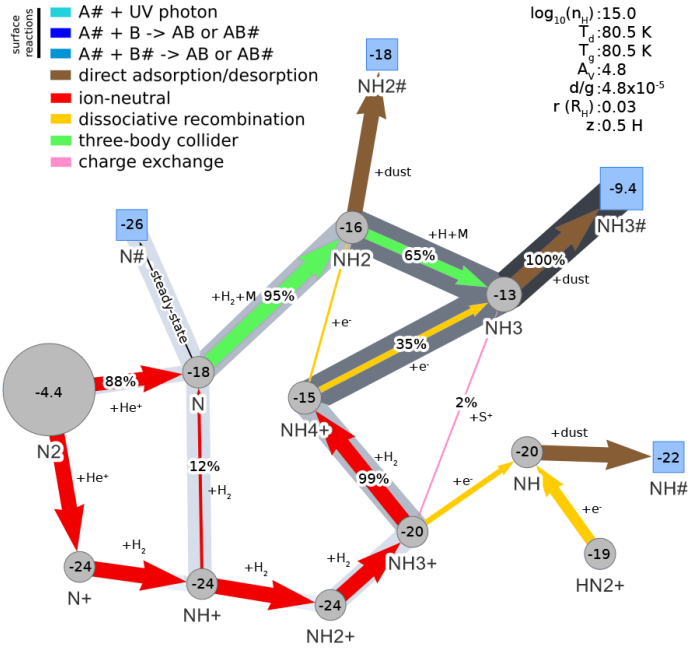

Fig. 6. Chemical network diagram illustrating the formation of NH_3 ice in the CPD after a partial reset, immediately prior to the accreted gas reaching the midplane. The pathway from N_2 to NH3# is highlighted. Percentages for reaction A→B indicate the fraction of reactions forming B which involve species A. A label "steady-state" indicates that the net rate is zero.

Near the midplane, NH_3 ice forms by direct adsorption from the gas phase onto dust grains. The gas-phase NH_3 originates primarily via a sequence of three body collider reactions:

$$H_2 + N + M \rightarrow NH_2 + M, \quad (18)$$

$$NH_2 + H + M \rightarrow NH_3 + M. \quad (19)$$

Here, M = H, H_2, or He. The importance of this pathway is illustrated clearly by the green arrows in the chemical network diagram in Fig. 6. These collider reactions are very efficient at the typical CPD midplane densities ($n_H \sim 10^{12}$ cm^{-3}). However, the absence of abundant atomic nitrogen prevents the collider pathway from producing significant quantities of NH_3. Then, N_2 is destroyed predominantly by reactions with He ions at a relatively low rate, as He+ is produced only be cosmic-ray ionization. The collider pathway to form NH_3 thus does not result in significant accumulation of NH_3 ice. By the time the gas parcel has reached the midplane, NH_3 ice is present only as a trace species.

The collider-pathway begins with the formation of NH_2 (Eq. (18)) which is also relevant to the water formation pathway involving $NH_2 + O \rightarrow NH + OH$ (Kamp et al. 2017). While the pre-exponential factor 10^{-26} cm^6 s^{-1} is derived from the work of Avramenko & Krasnen'kov (1966), we have chosen to adopt a significantly lower rate more typical of collider reactions (10^{-30} cm^6 s^{-1}), which still produces enough NH_2 for this path to be the dominant NH_3 formation route in the inner disk. It has been noted that this particular reaction is critical to accurately reproduce observed OH and H_2O gas-phase abundances, but that modern reevaluation of its rate and temperature dependence are needed (Kamp et al. 2017). For the second collider reaction in this path (Eq. (19)), we adopted the rate coefficients of Gordon et al. (1971), listing a pre-exponential factor 6.07×10^{-30} cm^6 s^{-1}. Other more recent experimental results assuming the reaction to be in the three body pressure regime give values

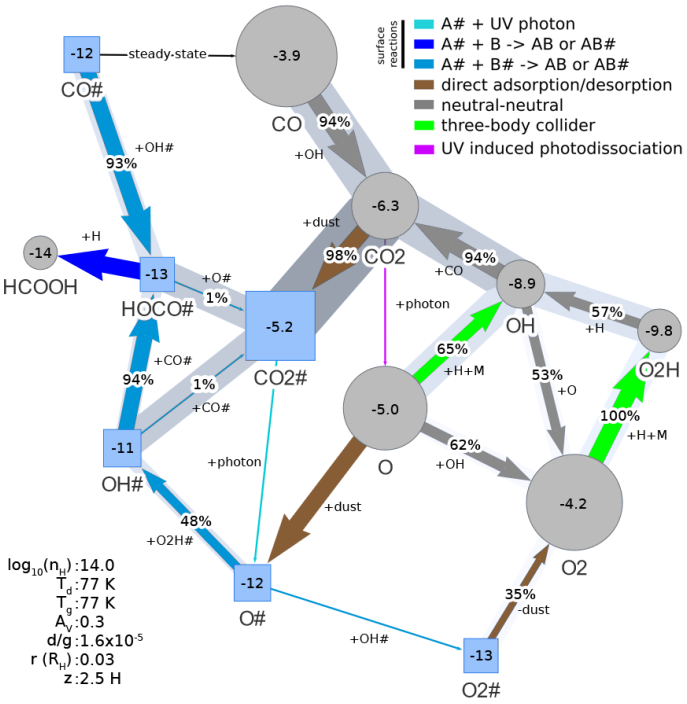

Fig. 7. Chemical reaction network illustrating the formation of CO_2 ice after a partial reset in which ices accreting onto the CPD are initially sublimated and placed into the gas-phase.

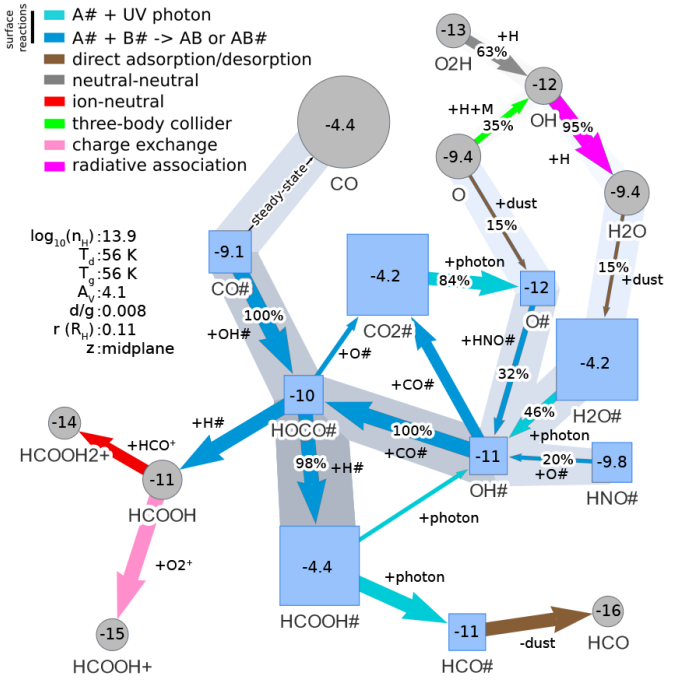

Fig. 8. Chemical network diagram centered on the formation of HCOOH ice in the outer regions of the CPD at the midplane.

in the range 2.3×10^{-30}–1.42×10^{-29} for various third bodies (Altinay & Macdonald 2012, 2015), hence, we consider this a reasonable value.

In the outer disk, NH_3 gas is efficiently photodissociated. The NH_3 ice is instead formed primarily by barrier-less successive hydrogenation of atomic nitrogen on icy grain surfaces (Charnley et al. 2001; Fedoseev et al. 2015) which has been experimentally demonstrated to occur (Hiraoka et al. 1995; Hidaka et al. 2011) via the Langmuir-Hinshelwood mechanism. The formation pathway is then

$$NH\# + H\# \rightarrow NH_2\#, \quad (20)$$
$$NH_2\# + H\# \rightarrow NH_3\#. \quad (21)$$

Both in the inner and outer disk NH_3 ice does not consitute more than 10^{-3} of the total ice by molar fraction.

3.1.2. Carbon dioxide (CO_2)

While CO_2 ice is initially only a trace species in the accreted circumstellar disk material, it becomes abundant in the CPD prior to the accreted material reaching the midplane. The chemical network diagram of the predominant CO_2 ice formation paths during this stage can be found in Fig. 7. This figure illustrates how the production of OH by collider reactions (green arrows) is critical to the efficient formation of CO_2 ice. In the time that accreted gas and ice reside in the optically thin surface layers of the CPD, it initially liberates significant quantities of atomic oxygen from gas-phase H_2O, which is hydrogenated via three-body collider reactions. The OH then reacts with abundant gas-phase CO to produce 98% of the CO_2, which then freezes out onto grains. In particular three-body collider reactions account for nearly all (>99%) OH formation which is critical for the CO+OH gas-phase reaction. It can also be seen in Fig. 7 that the grain-surface formation of CO_2 ice plays only a minor role prior to the gas parcel reaching the midplane.

After the gas and dust parcel reaches the midplane, the chemistry is evolved for an additional 10^3–10^4 yr for the high- and low-viscosity cases, respectively. The resulting composition at t_{visc} is similar to that of the full reset case, with the exception that the inner CPD (near the present day orbit of Callisto) also retains a significant CO_2 ice component. This can be seen in Figs. 5a,d. CO_2 ice formation continues in the outer CPD at the midplane in the absence of abundant atomic O, as OH is produced instead on grain-surfaces by the photodissociation of H2O#. This is described in the following section and can be seen in Fig. 8.

3.1.3. Formic acid (HCOOH)

HOCO (hydrocarboxyl radical) and HCOOH (formic acid) are of relevance in the cold, high-density midplane where CO_2 ice can form; thus, these were included in our extended chemical network. Formic acid is the simplest carboxylic acid and has been identified in star-forming regions (Schutte et al. 1999; Ikeda et al. 2001) both in gaseous and solid states, as well as in protoplanetary disks (Favre et al. 2018) and in comets (Crovisier et al. 2004). Its abundance typically varies with 1–10% of water ice (Bisschop et al. 2007).

The chemical network diagram of HCOOH formation in the outer CPD can be found in Fig. 8. It is clear that grain surface reactions play a completely dominant role in this process. In the outer CPD, we find that although it is not stable as an ice, the gas-phase CO freezes out and temporarily occupies a physisorption site on the grain surface. Prior to desorbing the CO# reacts on the grain surface OH# to form CO_2# and H# (Oba et al. 2010; Liu & Sander 2015), for which we have adopted the effective barrier of 150 K (Fulle et al. 1996; Ruaud et al. 2016).

$$CO + dust \rightarrow CO\#, \quad (22)$$
$$CO\# + OH\# \rightarrow CO_2\# + H\#. \quad (23)$$

Alternatively, as an intermediate step of the OH# + CO# reaction the van der Waals complex HOCO# is formed, which can be hydrogenated to form HCOOH#.

$$CO\# + OH\# \rightarrow HOCO\#, \quad (24)$$

$$HOCO\# + H\# \rightarrow HCOOH\#. \quad (25)$$

The HOCO# formation route can explain the presence of HCOOH# in cold, dense clouds (Ioppolo et al. 2011; Qasim et al. 2019). The resulting radial abundance of HCOOH# in the reference CPD can be seen in Fig. 5c. In the partial reset case, HCOOH ice can locally constitute a significant fraction of the ices in the reference CPD (∼10 mol%).

We found significant abundances (∼10% relative to H_2O ice) of HCOOH ice in the outer region of the CPD. This is comparable to the upper end of inferred abundances (∼1−10% level relative to H_2O ice) observed toward young stellar objects (Schutte et al. 1999; Keane et al. 2001; Knez et al. 2005; Boogert et al. 2015). The relatively large abundance of HCOOH ice in the outer CPD relative to its observationally derived abundance in astrophysical ice mixtures in the ISM is noteworthy. However, this was not entirely unexpected. The minimum CPD temperature set by equilibrium with the background radiation field ensures that a large region in the outer CPD exhibits a narrow range of temperature from 50–55 K. Given that the majority of the disk surface area is in this zone, the total disk composition is weighted heavily towards these specific conditions. However, background temperatures as low as 30 K or as high as 70 K do not produce abundant alternative impurities, while the outer CPD remains dominated by CO_2 and HCOOH ice.

Additionally, the stability of the HCOOH ice in our model is subject to several uncertainties. The only grain-surface reaction in our network that is able to destroy HCOOH# is the photo-induced dissociation to HCO# and OH#. Alternatively, it can be placed directly back into the gas phase by thermal, cosmic-ray, or UV-photon induced desorption. We did not include grain-surface hydrogenation of the HCOOH ice. Bisschop et al. (2007) found that hydrogen bombardment of a pure multilayer HCOOH ice does not result in the production of detectable reaction products, concluding that the hydrogenation of HCOOH does not play a role in formation of more complex species and that only minor amounts desorb. In contrast Chaabouni et al. (2020) found that H-bombardment of a <1−3 monolayer coating of HCOOH ice at 10–100 K results in efficient production of CO_2 and H_2O molecules, as well as CH_3OH and H_2CO. The authors suggest that this disagreement stems from the inefficiency of H atom diffusion through the pure HCOOH multilayer used in the experimental setup of Bisschop et al. (2007). Alternatively, the sub-monolayer conditions present in the setup of Chaabouni et al. (2020) potentially cause the substrate itself to become hydrogenated, increasing the sticking coefficient for H atoms and promoting surface reactions. Where HCOOH ice is found in our CPD, it has been co-deposited with H_2O ice and CO_2 ice (with molar ratio H_2O:CO_2:HCOOH 100:80:80), with an equivalent thickness of several hundred monolayers. Hence we consider it plausible that the majority of the HCOOH embedded within the ice matrix would not be efficiently hydrogenated.

Overall, HCOOH ice has not been detected on the surface of any Galilean moon. Experimental results indicate that HCOOH ice has a relatively short 8×10^7 yr half-life against irradiation by galactic cosmic rays, being dissociated into CO or CO_2 (Bergantini et al. 2013). Any HCOOH accreted onto the surface of, for instance, Callisto would therefore likely be absent in the present era, having reduced to <1% of its initial concentration within only 0.56 Gyr. There is a paucity of research investigating the role of HCOOH in subsurface melts, however, we know that under hydrothermal conditions, water can act as a homogeneous catalyst for the decarboxylation pathway of HCOOH decomposition in liquids (Ruelle et al. 1986), where it decomposes to become the astrobiologically relevant CO_2 and H_2 molecules (Yu & Savage 1998).

3.2. Full reset (initially atomic gas)

In the full reset case, the gas in the CPD is initially fully atomic and ionized and no ices are present. This state represents, for instance, the accretion of a high-mass planet ($M > 1\ M_J$), with correspondingly higher infall shock-velocity at the CPD surface, or an accretion of material originating from a greater scale height in the circumstellar disk than we have considered. In the fully reset case, the abundant free atomic hydrogen enables highly efficient combustion chemistry to produce a water-dominated ice composition, as found in Paper I. This efficient water formation locks away the majority of atomic oxygen early on and it is 10^5 times less abundant than in the partial reset case after 5 yr. Accordingly, the OH formation rate via O+H is lower and so significantly less OH is available to form CO_2 via CO+OH, while the CO abundances are very similar between the two cases ($10^{-3.86}$ vs. $10^{-3.88}$ relative to H_2).

Again, ammonia ice is not able to form in abundance as the initially atomic nitrogen is predominantly locked in N_2 within a single year via N + NO →N_2 + O or N + NH →N_2 + H. The radial composition of the ices after 10^4 yr is similar to the partial reset case, although CO_2 ice is found in abundance only in the outer disk beyond ∼ 2× the semi-major axis of Callisto.

In contrast to the partial reset case, the inner disk region is dominated by water ice with a minor (<1%) methanol (CH_3OH) component. Methanol is an important primordial solar system volatile and may act as an anti-freeze in subsurface oceans (Deschamps et al. 2010; Dougherty et al. 2018). It has been found to be abundant in solid form near protostars (Dartois et al. 1999; Boogert et al. 2015), in comets (Bockelee-Morvan et al. 1991; Mumma et al. 1993; Bockelée-Morvan & Biver 2017; Biver & Bockelée-Morvan 2019), and in the gas-phase in planet-forming disks (Walsh et al. 2016; Booth et al. 2021), where it may be formed via grain-surface reactions involving hydrogenation of CO# (Hiraoka et al. 1994; Watanabe & Kouchi 2002). At typical pressures in our reference CPD the freeze-out temperature of methanol is greater than that of NH_3 and CO_2 (Mousis et al. 2009; Johnson et al. 2012). Thus, if the CO_2 ice observed on Callisto's surface was formed primordially in the CPD, we could expect that temperatures in the CPD could have allowed for stable methanol ice to be present as well. Indeed, we find that in the inner disk this occurs for $t_{visc} > 10^3$ yr, where methanol ice is present at the 1% level at temperatures above 65 K with a peak abundance at 95–100 K. At these densities, it originates almost exclusively from reactions in the gas-phase via sequential hydrogenation of CO in two- and three-body reactions. Approximately 70% is formed via:

$$CO + H + M \rightarrow HCO + M, \quad (26)$$

$$HCO + H + M \rightarrow H_2CO + M, \quad (27)$$

$$H_2CO + H \rightarrow CH_3O, \quad (28)$$

$$CH_3O + H \rightarrow CH_3OH, \quad (29)$$

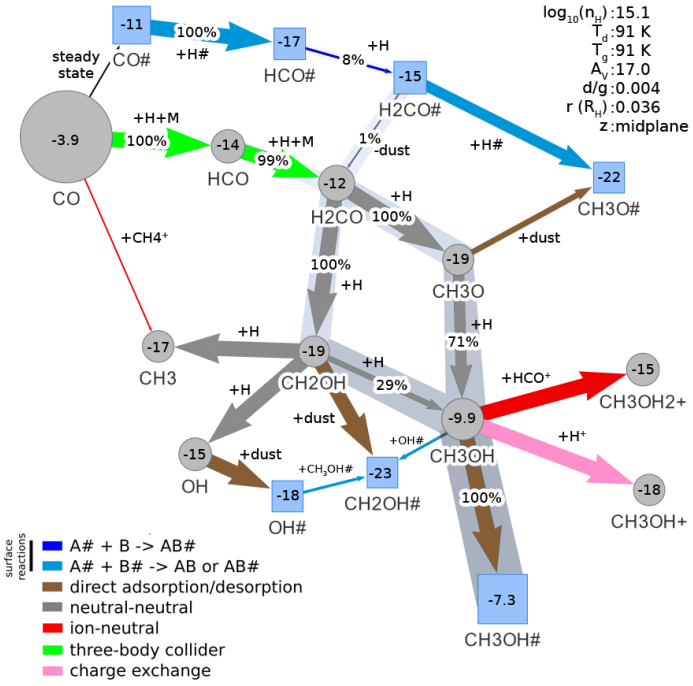

Fig. 9. Chemical network diagram centered on the formation of CH_3OH at the CPD midplane in the reset case.

and the remainder by

$$H_2CO + H \rightarrow CH_2OH, \quad (30)$$

$$CH_2OH + H \rightarrow CH_3OH. \quad (31)$$

For the reaction $H_2CO \rightarrow CH_3OH$, we have adopted the rate coefficients from Huynh & Violi (2008) with a barrier of 865 K. In the absence of this reaction, we find that methanol is produced in similar quantities via the CH_2OH pathway. The rate of formation is thus highly contingent on the availability of free atomic hydrogen in the gas-phase. The absence of abundant atomic hydrogen prevents the accumulation of methanol in the partial reset or inheritance cases. An additional "bottleneck" in the reaction network is H_2CO. This can be seen in Fig. 9. H_2CO is formed almost exclusively (>99%) via gas-phase three-body collider reactions.

In the ISM, methanol ice abundances can significantly exceed that which we find in the CPD. The grain-surface hydrogenation of H_2CO to form CH_3O (Eq. (28)) has been observed at low temperatures experimentally (Hidaka et al. 2004; Fuchs et al. 2009; Chuang et al. 2016), suggesting that successive hydrogenations of CO can explain the observed abundance of interstellar methanol at low temperatures (<15 K). Above this temperature the desorption of H atoms and lower sticking efficiency of H due to the absence of H_2 causes a considerable drop in this reaction rate. While these reactions are included in our chemical network, the gas temperature in the CPD does not fall below 50 K; thus, we find this path to be inefficient.

3.3. Full inheritance case

In the event of a full chemical inheritance from the circumstellar disk gap edge, the ice accreting onto the CPD consists predominantly of water, with ratios H_2O:NH_3:HCN of 100:15:10 and a significant ~10% component of hydrocarbon ices (e.g. C_2H_2, C_3H_2). This result is generally consistent with modeling of the outer regions of the circumstellar disk where $NH_3/H_2O = 0.14$ with as much as 80% of the nitrogen locked into NH_3 and to a lesser extent HCN (Dodson-Robinson et al. 2009).

The final composition of the ices in the inheritance scenario is highly contingent on their initial composition. Given the difficulties in correctly capturing the relevant physical conditions at the outer gap edge and the uncertainty from which altitude the gas originates, we consider it more informative to discuss how the ices are altered post-accretion, rather than focusing on their final composition.

Some minor processing of the ices occurs once they are incorporated into the CPD. The more volatile HCN and hydrocarbon ices are lost in the inner region of the disk where only NH_3# and a minor component of hydrocarbon ices remain as impurities. In the outer region of the CPD, some conversion of H_2O and HCN to HCOOH occurs, and to a minor extent CO_2.

At temperature below 70 K HCOOH is co-deposited with the NH_3 ice. In the presence of the proton acceptor NH_3, HCOOH will convert to the formate anion $HCOO^-$ and $NH4^+$ (Hudson & Moore 1999; Schutte et al. 1999; Gálvez et al. 2010) however formate is not included in our chemical network. Likewise the salt formation reaction is not included in the network. We consider what impact the inclusion of this process could have on our final derived abundances. While the activation barrier of the reaction is negligible, the barrier against diffusion prevents it from occurring at 50–70 K (Schutte et al. 1999). However some of the HCOOH will react immediately upon deposition due to the acid and base being in direct contact at adjacent binding sites. 10% of the HCOOH ice is observed to react promptly at 10 K in H_2O-NH_3-HCOOH mixtures with equal parts NH_3-HCOOH (Schutte et al. 1999). Hence we might expect that as much as ~20% of the HCOOH present in the outer disk could be converted upon adsorption to HCOO-NH_4+.

3.4. Differing diffusion timescales

Owing to the uncertainity in the diffusion timescale on which the gas parcel drifts towards the CPD midplane we considered also the case of 10× shorter and longer t_{diff}. For t_{diff} = 100 yr all three initial conditions converge towards a similar final composition which is CO_2-dominated (>95% by weight) across the entire disk. This is clearly inconsistent with observations of the Galilean moons. The shorter t_{diff} = 1 yr leaves the chemistry less affected by the time spent at the disk surface. In the partial reset case, a minor fraction (3%) of the accreted circumstellar NH_3 ice survives and can still be found at the CPD midplane after 10^4 yr. In the full reset case, the CH_3OH component in the inner disk region becomes more substantial, increasing to a peak of 4% of the total ice mass. This additional CH_3OH forms because more of the initially atomic hydrogen survives until ices become stable against photodissociation, and are available to hydrogenate H_2CO and CH_3O.

4. Implications

4.1. Absence of ammonia as an indicator of chemical reset

We have found that a partial or complete chemical reset of the CPD tends to suppress NH_3 formation as efficient N_2 self-shielding locks up nitrogen in N_2. Even if a substantial component (~20–30%) of NH_3 ice were present in Jupiter's feeding zone, a partial or complete reset would prevent its accumulation in the building blocks of the moons. Without a substantial NH_3 component the liquidus temperature of the Galilean subsurface oceans may not differ substantially from that of a pure water

ice. Europa appears to be the only Galilean moon where tectonic or cryovolcanic processes have recently exchanged material between the surface and subsurface where it could provide clues to composition of an ocean (Kargel et al. 2000; Zolotov & Shock 2001). NH_3 brought to the surface in the form of an NH_3-H_2O matrix could be lost on geologically brief timescales to external radiation (Moore et al. 2007; Bergantini et al. 2014). Longevity of surface ammonia might be extended if it would appear in a more stable form such as a hydrate or salt (Cook et al. 2018) but no positive detection has thus far been made (Clark et al. 2014). The non-detection of ammonium compounds on Europa's surface is compatible with a lack of ammonia in a subsurface ocean, although is certainly not conclusive evidence of its absence.

In contrast to the Galilean system, several lines of evidence indicate the presence of NH_3 ice during the accretion of the Saturnian moons. The inferred interior composition of the Saturnian moon Enceladus appears to resemble more closely well-mixed outer solar system material and is generally consistent with a composition inherited from solar nebular (cometary) material (Waite et al. 2009). Enceladus contains a liquid water ocean (Thomas et al. 2016) from which interior material is ejected through plumes (Spahn et al. 2006; Porco et al. 2006; Waite et al. 2006). The presence of NH_3 in the plumes of Enceladus has been established by measurements from several instruments onboard the Cassini spacecraft (Waite et al. 2009) at $4 > 0.1\%$ relative to H_2O, besides CO_2, CH_4 and H_2 (Magee & Waite 2017). Likewise NH_3 ice is considered to be a likely source of Titan's nitrogen (McKay et al. 1988; Sekine et al. 2011; Mandt et al. 2014).

We suggest that the CPDs of sufficiently massive planets lose accreted NH_3 ice to mild accretion shocks and subsequent chemical evolution, and that the absence of NH_3 ice may indicate a (partial) chemical reset has occurred. As NH_3 represents one of the most potent and potentially abundant anti-freezes, subsurface ocean occurrence rates and longevity may then be relatively enhanced in the icy moons that accompany lower-mass giant planets which inherit circumstellar material.

4.2. Carbon Dioxide at the origin of Ganymede and Callisto

Several lines of evidence suggest the surface of Callisto is among the most primordial of the regular satellites, potentially providing a direct link to the formation environment of the Galilean moons (Moore et al. 2004; Zahnle et al. 2003). CO_2 ice has been detected on the surface of both Ganymede and Callisto (Carlson et al. 1996; McCord et al. 1997) but only appears below the surface on Callisto (Hibbitts et al. 2002, 2003), where it appears to be exhumed by impact cratering. In contrast, CO_2 on the surface of Ganymede appears to be of exogeneous or radiolitic origin (Hibbitts et al. 2003). Hence if we consider Callisto's reservoir of CO_2 ice to be primordial we can consider which of our assumptions are consistent with its presence.

In the partial reset case, which we considered to be a priori the most likely initial condition of accreted material, CO_2 ice is present in significant quantities at the present-day position of Callisto but less so near Ganymede. Superficially this appears to be consistent with the proposed distinct origins of Ganymede and Callisto's CO_2. However, the local ice mass fraction of CO_2 in the CPD is high ($\geq$60%). This appears to be in conflict with the inferred surface abundance of CO_2 ice on Callisto, where it constitutes no more than 0.01–0.16% of the host material mass (Hibbitts et al. 2002). It is however unclear whether the observationally inferred surface abundance of CO_2 on Callisto is truly representative of the subsurface composition. Pure CO_2 ice is not stable at the surface of the Galilean moons and CO_2 may instead be present in the form of clathrates (Chaban et al. 2007). Hence, an initially large CO_2 component exposed to the surface could have been lost to sublimation and dissociation. A substantial subsurface CO_2 reservoir is nevertheless implied, given the continuous replenishment of Callisto's CO_2 exosphere (Carlson 1999). In contrast to the partially reset case, we find CO_2 ice at a concentration of ~0.2% near Callisto's location in the fully reset CPD. While this appears to be more representative of what is known of the Galilean moon surface composition, the primordial CO_2 concentration of Callisto's building blocks cannot simply be derived from the present state of the surface.

Our findings are consistent with a primordial origin for Callisto's CO_2, and point to the possibility that Ganymede and Callisto's icy building blocks had distinct chemical compositions. While it has been suggested that Ganymede may have formed with a primordial CO_2 component which was lost during an episodic period of surface melting, our results suggest icy grains in its vicinity were CO_2-poor. A CPD midplane temperature profile which is dominated by viscous heating and in which the water iceline falls between Europa and Ganymede naturally produces a CO_2 iceline between Ganymede and Callisto.

5. Summary and conclusions

If CPD ice composition is (partially or fully) reset, NH_3 ice formation is inefficient due to N_2 self-shielding. The resulting $\ll$1% concentration of NH_3 ice is unlikely to significantly alter the thermophysical/chemical properties of subsurface melt. The most significant impurities are the carbon-bearing CO_2 and HCOOH ices and each make up at most ~10% of the molar ice fraction. If the growth of the Galilean moons occurred near their present-day positions they are largely free of impurities, being composed of 98% water ice, ~2% CH_3OH, and trace amounts of CO_2. If instead the CPD ice composition is inherited from the circumstellar nebula, NH_3 ice can survive conditions at the CPD midplane and becomes the most abundant impurity. Observations indicating the presence of NH_3 in the Saturnian satellite system but not in the Galilean one are consistent with a reset-inheritance dichotomy. NH_3 in the planetary feeding zone of Jupiter, if present, may have been destroyed during accretion onto the CPD and then could not form again in time. Our key findings are summarized as follows:

1. The ice composition of the Galilean moons corresponds to a partial or full chemical reset, as opposed to the ices of the Saturnian moons, which may have been more directly inherited from the circumstellar disk.
2. A partial reset prevents efficient formation of ammonia ice. The building blocks of the Galilean moons (and of exomoons forming in similar CPDs) would be nitrogen-poor (NH_3 ice abundances with respect to the H_2O ice of ~0.1%).
3. Our results are consistent with a primordial origin for CO_2 ice on Callisto and an ice composition that is chemically distinct from Ganymede. Please add 2–3 sentences of a general conclusion following these points.

The composition of the building blocks that form moons around giant planets is determined by the conditions of accretion onto the planet's CPD, which in turn is influenced by the mass and orbital properties of the planet. The compositional reset-inheritance dichotomy of CPD ices ties together the properties of the planet and the long-term geophysical evolution and composition of icy satellite interior oceans.

Acknowledgements. The research of N.O. and I.K. is supported by grants from the Netherlands Organization for Scientific Research (NWO, grant number 614.001.552) and the Netherlands Research School for Astronomy (NOVA). This research has made use of NASA's Astrophysics Data System Bibliographic Services. This research has also extensively used Numpy (Harris et al. 2020), Matplotlib (Hunter 2007), Scipy (Virtanen et al. 2020), and Prodimopy `https://gitlab.astro.rug.nl/prodimo/prodimopy`. N.O. would like to thank S. Ceulemans for her suggestion that greatly improved the visualizations in this work, as well as J. Tjoa and S. van Mierlo for helpful discussions and support.

References

Altinay, G., & Macdonald, R. G. 2012, J. Phys. Chem. A, 116, 2161
Altinay, G., & Macdonald, R. G. 2015, J. Phys. Chem. A, 119, 7593
Aota, T., Inoue, T., & Aikawa, Y. 2015, ApJ, 799, 141
Aoyama, Y., Ikoma, M., & Tanigawa, T. 2018, ApJ, 866, 84
Avramenko, L. I., & Krasnen'kov, V. M. 1966, Bull. Acad. Sci. USSR, 15, 394
Ayliffe, B. A., & Bate, M. R. 2009, MNRAS, 397, 657
Barlow, M. J., & Silk, J. 1976, ApJ, 207, 131
Batygin, K., & Morbidelli, A. 2020, ApJ, 894, 143
Bauschlicher, Charles W., J. 1998, ApJ, 509, L125
Bell, R. 1980, The Tunnel Effect in Chemistry (USA: Springer)
Bergantini, A., Pilling, S., Rothard, H., Boduch, P., & Andrade, D. P. P. 2013, MNRAS, 437, 2720
Bergantini, A., Pilling, S., Nair, B. G., Mason, N. J., & Fraser, H. J. 2014, A&A, 570, A120
Bisschop, S. E., Fuchs, G. W., Boogert, A. C. A., van Dishoeck, E. F., & Linnartz, H. 2007, A&A, 470, 749
Bitsch, B., Morbidelli, A., Johansen, A., et al. 2018, A&A, 612, A30
Biver, N., & Bockelée-Morvan, D. 2019, ACS Earth Space Chem., 3, 1550
Bockelée-Morvan, D., & Biver, N. 2017, Philos. Trans. R. Soc. London Ser. A, 375, 20160252
Bockelee-Morvan, D., Colom, P., Crovisier, J., Despois, D., & Paubert, G. 1991, Nature, 350, 318
Bonfanti, M., & Martinazzo, R. 2016, Int. J. Quantum Chem., 116, 1575
Boogert, A. C. A., Gerakines, P. A., & Whittet, D. C. B. 2015, ARA&A, 53, 541
Booth, A. S., Walsh, C., Terwisscha van Scheltinga, J., et al. 2021, Nat. Astron., 5, 684
Boschman, L., Reitsma, G., Cazaux, S., et al. 2012, ApJ, 761, L33
Canup, R. M., & Ward, W. R. 2002, AJ, 124, 3404
Canup, R. M., & Ward, W. R. 2006, Nature, 441, 834
Carlson, R. W. 1999, Science, 283, 820
Carlson, R., Smythe, W., Baines, K., et al. 1996, Science, 274, 385
Carlson, R. W., Kargel, J. S., Douté, S., Soderblom, L. A., & Dalton, J. B. 2007, in Io After Galileo: a New View of Jupiter's Volcanic Moon, eds. R. M. C. Lopes, & J. R. Spencer (Berlin: Springer), 193
Carr, M. H., Belton, M. J. S., Chapman, C. R., et al. 1998, Nature, 391, 363
Caselli, P., Stantcheva, T., & Herbst, E. 2004, in The Dense Interstellar Medium in Galaxies, eds. S. Pfalzner, C. Kramer, C. Straubmeier, & A. Heithausen (Berlin, Heidelberg: Springer), 479
Cazaux, S., & Tielens, A. G. G. M. 2002, ApJ, 575, L29
Cazaux, S., Boschman, L., Rougeau, N., et al. 2016, Sci. Rep., 6, 19835
Chaabouni, H., Baouche, S., Diana, S., & Minissale, M. 2020, A&A, 636, A4
Chaban, G. M., Bernstein, M., & Cruikshank, D. P. 2007, Icarus, 187, 592
Charnley, S. B., Rodgers, S. D., & Ehrenfreund, P. 2001, A&A, 378, 1024
Choukroun, M., & Grasset, O. 2010, J. Chem. Phys., 133, 144502
Chuang, K. J., Fedoseev, G., Ioppolo, S., van Dishoeck, E. F., & Linnartz, H. 2016, MNRAS, 455, 1702
Clark, R. N., Swayze, G. A., Carlson, R., Grundy, W., & Noll, K. 2014, Rev. Mineral. Geochem., 78, 399
Cook, J. C., Ore, C. M. D., Protopapa, S., et al. 2018, Icarus, 315, 30
Croft, S. K., Lunine, J. I., & Kargel, J. 1988, Icarus, 73, 279
Crovisier, J., Bockelée-Morvan, D., Colom, P., et al. 2004, A&A, 418, 1141
D'Alessio, P., Canto, J., Calvet, N., & Lizano, S. 1998, ApJ, 500, 411
Dartois, E., Schutte, W., Geballe, T. R., et al. 1999, A&A, 342, L32
Davidson, D., Petersen, E., Röhrig, M., Hanson, R., & Bowman, C. 1996, Symp. Int. Combus., 26, 481
Desch, S. J., Cook, J. C., Doggett, T. C., & Porter, S. B. 2009, Icarus, 202, 694
Deschamps, F., Mousis, O., Sanchez-Valle, C., & Lunine, J. I. 2010, ApJ, 724, 887
Dodson-Robinson, S. E., Willacy, K., Bodenheimer, P., Turner, N. J., & Beichman, C. A. 2009, Icarus, 200, 672
Dougherty, A. J., Bartholet, Z. T., Chumsky, R. J., et al. 2018, J. Geophys. Res. Planets, 123, 3080
Draine, B. T., & McKee, C. F. 1993, ARA&A, 31, 373
Favre, C., Fedele, D., Semenov, D., et al. 2018, ApJ, 862, L2
Fedoseev, G., Ioppolo, S., Zhao, D., Lamberts, T., & Linnartz, H. 2015, MNRAS, 446, 439
Frank, J., King, A., & Raine, D. J. 2002, Accretion Power in Astrophysics, 3rd edn. (Cambridge, UK: Cambridge University Press)
Fuchs, G. W., Cuppen, H. M., Ioppolo, S., et al. 2009, A&A, 505, 629
Fulle, D., Hamann, H. F., Hippler, H., & Troe, J. 1996, J. Chem. Phys., 105, 983
Gálvez, O., Maté, B., Herrero, V. J., & Escribano, R. 2010, ApJ, 724, 539
Garrod, R. T., & Herbst, E. 2006, A&A, 457, 927
Garrod, R. T., & Pauly, T. 2011, ApJ, 735, 15
Garrod, R., Park, I. H., Caselli, P., & Herbst, E. 2006, Faraday Discuss., 133, 51
Glein, C. R. 2015, Icarus, 250, 570
Gordon, S., Mulac, W., & Nangia, P. 1971, J. Phys. Chem., 75, 2087
Grasset, O., Sotin, C., & Deschamps, F. 2000, Planet. Space Sci., 48, 617
Hahn, J., Krasnoperov, L., Luther, K., & Troe, J. 2004, Phys. Chem. Chem. Phys., 6, 1997
Hammond, N. P., Parmenteir, E. M., & Barr, A. C. 2018, J. Geophys. Res. Planets, 123, 3105
Harris, C. R., Millman, K. J., van der Walt, S. J., et al. 2020, Nature, 585, 357
Hart, M. H. 1979, Icarus, 37, 351
Hasegawa, T. I., & Herbst, E. 1993, MNRAS, 261, 83
Hasegawa, T. I., Herbst, E., & Leung, C. M. 1992, ApJS, 82, 167
Hayashi, C., Nakazawa, K., & Nakagawa, Y. 1985, in Protostars and Planets II, eds. D. C. Black, & M. S. Matthews (Tucson: University of Arizona Press), 1100
Hibbitts, C. A., Klemaszewski, J. E., McCord, T. B., Hansen, G. B., & Greeley, R. 2002, J. Geophys. Res. Planets, 107, 14
Hibbitts, C. A., Pappalardo, R. T., Hansen, G. B., & McCord, T. B. 2003, J. Geophys. Res. Planets, 108, 5036
Hidaka, H., Watanabe, N., Shiraki, T., Nagaoka, A., & Kouchi, A. 2004, ApJ, 614, 1124
Hidaka, H., Watanabe, M., Kouchi, A., & Watanabe, N. 2011, Phys. Chem. Chem. Phys., 13, 15798
Hirama, M., Tokosumi, T., Ishida, T., & Aihara, J.-i. 2004, Chem. Phys., 305, 307
Hiraoka, K., Ohashi, N., Kihara, Y., et al. 1994, Chem. Phys. Lett., 229, 408
Hiraoka, K., Yamashita, A., Yachi, Y., et al. 1995, ApJ, 443, 363
Horowitz, A. 1985, J. Phys. Chem., 89, 1764
Hudson, R. L., & Moore, M. H. 1999, Icarus, 140, 451
Hunter, J. D. 2007, Comput. Sci. Eng., 9, 90
Hussmann, H., & Spohn, T. 2004, Icarus, 171, 391
Hussmann, H., Sohl, F., & Spohn, T. 2006, Icarus, 185, 258
Huynh, L. K., & Violi, A. 2008, J. Organic Chem., 73, 94
Ikeda, M., Ohishi, M., Nummelin, A., et al. 2001, ApJ, 560, 792
Ioppolo, S., Cuppen, H. M., van Dishoeck, E. F., & Linnartz, H. 2011, MNRAS, 410, 1089
Johnson, T. V., Mousis, O., Lunine, J. I., & Madhusudhan, N. 2012, ApJ, 757, 192
Kamp, I., Thi, W. F., Woitke, P., et al. 2017, A&A, 607, A41
Kamp, I., Tilling, I., Woitke, P., Thi, W. F., & Hogerheijde, M. 2010, A&A, 510, A18
Kargel, J. S. 1992, Icarus, 100, 556
Kargel, J. S., Kaye, J. Z., Head, J. W., et al. 2000, Icarus, 148, 226
Keane, J. V., Tielens, A. G. G. M., Boogert, A. C. A., Schutte, W. A., & Whittet, D. C. B. 2001, A&A, 376, 254
Khurana, K. K., Kivelson, M. G., Stevenson, D. J., et al. 1998, Nature, 395, 777
Kirk, R., & Stevenson, D. 1987, Icarus, 69, 91
Kivelson, M. G., Khurana, K. K., & Volwerk, M. 2002, Icarus, 157, 507
Knez, C., Boogert, A. C. A., Pontoppidan, K. M., et al. 2005, ApJ, 635, L145
Kurylo, M. J. 1972, J. Phys. Chem., 76, 3518
Leliwa-Kopystyński, J., Maruyama, M., & Nakajima, T. 2002, Icarus, 159, 518
Li, X., Heays, A. N., Visser, R., et al. 2013, A&A, 555, A14
Liu, Y., & Sander, S. 2015, J. Phys. Chem. A, 119, 571
Machida, M. N., Kokubo, E., Inutsuka, S.-i., & Matsumoto, T. 2008, ApJ, 685, 1220
Magee, B., & Waite, J. 2017, Lunar Planet. Sci. Conf., 1964, 2974
Mandt, K. E., Mousis, O., Lunine, J., & Gautier, D. 2014, ApJ, 788, L24
Martin, R. G., & Lubow, S. H. 2011, MNRAS, 413, 1447
McCord, T. B., Carlson, R., Smythe, W., et al. 1997, Science, 278, 271
McElroy, D., Walsh, C., Markwick, A. J., et al. 2013, A&A, 550, A36
McKay, C. P., Scattergood, T. W., Pollack, J. B., Borucki, W. J., & van Ghyseghem, H. T. 1988, Nature, 332, 520
Mennella, V., Hornekær, L., Thrower, J., & Accolla, M. 2012, ApJ, 745, L2
Mertens, J., Kalitan, D., Barrett, A., & Petersen, E. 2009, Proc. Combus. Inst., 32, 295
Moore, J. M., Chapman, C. R., Bierhaus, E. B., et al. 2004, in Jupiter. The Planet, Satellites and Magnetosphere, eds. F. Bagenal, T. E. Dowling, & W. B. McKinnon (Cambridge: Cambridge University Press), 1, 397
Moore, M., Ferrante, R., Hudson, R., & Stone, J. 2007, Icarus, 190, 260

Morbidelli, A., & Nesvorny, D. 2012, A&A, 546, A18
Morii, Y., Tsuboi, N., Koshi, M., et al. 2009, Sci. Technol. Energetic Mater., 70, 117
Mousis, O., & Alibert, Y. 2006, A&A, 448, 771
Mousis, O., Alibert, Y., Sekine, Y., Sugita, S., & Matsui, T. 2006, A&A, 459, 965
Mousis, O., Lunine, J. I., Thomas, C., et al. 2009, ApJ, 691, 1780
Mumma, M. J., Hoban, S., Reuter, D. C., & Disanti, M. 1993, AAS/Div. Planet. Sci. Meeting Abs., 25, 14.10
Nimmo, F., & Pappalardo, R. T. 2016, J. Geophys. Res. Planets, 121, 1378
Oba, Y., Watanabe, N., Kouchi, A., Hama, T., & Pirronello, V. 2010, ApJ, 712, L174
Öberg, K. I., Garrod, R. T., van Dishoeck, E. F., & Linnartz, H. 2009, A&A, 504, 891
Oberg, N., Kamp, I., Cazaux, S., Woitke, P., & Thi, W. F. 2022, A&A, 667, A95
Peale, S. J., & Lee, M. H. 2002, Science, 298, 593
Perrone, G., Unpingco, J., & Lu, H.-m. 2020, ArXiv e-prints [arXiv:2006.04951]
Porco, C. C., Helfenstein, P., Thomas, P. C., et al. 2006, Science, 311, 1393
Qasim, D., Lamberts, T., He, J., et al. 2019, A&A, 626, A118
Quillen, A. C., & Trilling, D. E. 1998, ApJ, 508, 707
Rauls, E., & Hornekær, L. 2008, ApJ, 679, 531
Reboussin, L., Wakelam, V., Guilloteau, S., & Hersant, F. 2014, MNRAS, 440, 3557
Rice, W. K. M., Armitage, P. J., Wood, K., & Lodato, G. 2006, MNRAS, 373, 1619
Ruaud, M., Loison, J. C., Hickson, K. M., et al. 2015, MNRAS, 447, 4004
Ruaud, M., Wakelam, V., & Hersant, F. 2016, MNRAS, 459, 3756
Ruelle, P., Kesselring, U. W., & Nam-Tran, H. 1986, J. Am. Chem. Soc., 108, 371
Saur, J., Duling, S., Roth, L., et al. 2015, J. Geophys. Res. Space Phys., 120, 1715
Schutte, W. A., Boogert, A. C. A., Tielens, A. G. G. M., et al. 1999, A&A, 343, 966
Sekine, Y., Genda, H., Sugita, S., Kadono, T., & Matsui, T. 2011, Nat. Geosci., 4, 359
Sekine, Y., Genda, H., Muto, Y., et al. 2014, Icarus, 243, 39
Sellevåg, S. R., Georgievskii, Y., & Miller, J. A. 2008, J. Phys. Chem. A, 112, 5085
Showman, A. P., & Malhotra, R. 1999, Science, 296, 77
Showman, A. P., Stevenson, D. J., & Malhotra, R. 1997, Icarus, 129, 367
Sohl, F., Spohn, T., Breuer, D., & Nagel, K. 2002, Icarus, 157, 104
Sohl, F., Choukroun, M., Kargel, J., et al. 2010, Space Sci. Rev., 153, 485
Spahn, F., Schmidt, J., Albers, N., et al. 2006, Science, 311, 1416
Spohn, T., & Schubert, G. 2003, Icarus, 161, 456
Szulágyi, J. 2017, ApJ, 842, 103
Szulágyi, J., & Mordasini, C. 2017, MNRAS, 465, L64
Takasao, S., Aoyama, Y., & Ikoma, M. 2021, ApJ, 921, 10
Thi, W. F., Woitke, P., & Kamp, I. 2011, MNRAS, 412, 711
Thi, W. F., Hocuk, S., Kamp, I., et al. 2020, A&A, 634, A42
Thomas, P. C., Tajeddine, R., Tiscareno, M. S., et al. 2016, Icarus, 264, 37
Thrower, J. D., Collings, M. P., Rutten, F. J. M., & McCoustra, M. R. S. 2009, MNRAS, 394, 1510
Thrower, J. D., Jørgensen, B., Friis, E. E., et al. 2012, ApJ, 752, 3
Tielens, A. G. G. M. 2005, The Physics and Chemistry of the Interstellar Medium (Cambridge: Cambridge University Press)
Tielens, A. G. G. M. 2021, Molecular Astrophysics (Cambridge: Cambridge University Press)
Vance, S. D., Panning, M. P., Stähler, S., et al. 2018, J. Geophys. Res. Planets, 123, 180
van Dishoeck, E. F., & Blake, G. A. 1998, ARA&A, 36, 317
Virtanen, P., Gommers, R., Oliphant, T. E., et al. 2020, Nat. Methods, 17, 261
Waite, J. H., Combi, M. R., Ip, W.-H., et al. 2006, Science, 311, 1419
Waite, J. H., Jr., Lewis, W. S., Magee, B. A., et al. 2009, Nature, 460, 487
Wakelam, V., Bron, E., Cazaux, S., et al. 2017, Mol. Astrophys., 9, 1
Walsh, C., Loomis, R. A., Öberg, K. I., et al. 2016, ApJ, 823, L10
Watanabe, N., & Kouchi, A. 2002, ApJ, 571, L173
Woitke, P., Dominik, C., & Sedlmayr, E. 1993, A&A, 274, 451
Woitke, P., Kamp, I., & Thi, W.-F. 2009, A&A, 501, 383
Woitke, P., Min, M., Pinte, C., et al. 2016, A&A, 586, A103
Woodall, J., Agúndez, M., Markwick-Kemper, A. J., & Millar, T. J. 2007, A&A, 466, 1197
Yu, J., & Savage, P. E. 1998, Industrial Eng. Chem. Res., 37, 2
Zahnle, K., Schenk, P., Levison, H., & Dones, L. 2003, Icarus, 163, 263
Zhu, Z., Nelson, R. P., Dong, R., Espaillat, C., & Hartmann, L. 2012, ApJ, 755, 6
Zolotov, M. Y., & Shock, E. L. 2001, J. Geophys. Res., 106, 32815

Appendix A: Chemical network diagrams annotated

The chemical network diagrams are generated algorithmically according to the following rules:

1. A single species is selected as the seed from which the diagram will be generated.
2. In the first iteration, all species which are involved in the formation or destruction of the seed above a certain rate threshold are added as nodes to the network (one degree of separation).
3. The reaction with the highest rate relating two species is represented as a connection (arrow) between the two nodes.
4. This process is iterated starting from (2) for n degrees of separation.

An annotated example chemical network diagram can be found in Fig. A.1. While one species may be involved in the formation of another through multiple distinct reactions (i.e. H+OH→H_2O and OH+OH→H_2O+O), we color code the reaction connecting the nodes with the type (i.e. ion-neutral) of the reaction with the highest rate v. The arrow width is proportional to the net formation rate (v(A→B) - v(B→A)) between the two species. The node size is proportional to the abundance of the species. For some reactions the fraction of the reactions forming species B involving species A is included as a percentage (i.e. for A→B 20% of all the reactions that form B involves A). Networks are generated for a single grid point in the CPD model (ambient conditions are listed in the respective diagram) and at a specific time only, and are thus to be considered as "snapshots". H and H_2 are not displayed as nodes. Arrows are not displayed if they contribute less than 1% to the total formation rate of a species.

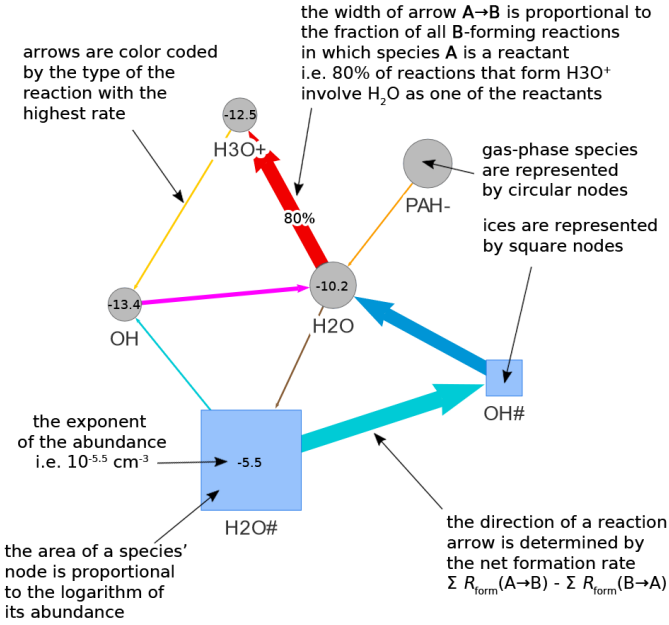

Fig. A.1: Example chemical network diagram with annotations describing how the diagram can be interpreted. The primary formation pathway of a species may also be highlighted for reference (not depicted).

Appendix B: Initial chemical abundances

The top 10 most abundant species for each chemical initial condition can be found in Table B.1 normalized to the most common species.

Table B.1: Abundance* of the 10 most common species for each initial condition.

Reset		Partial Reset		Inherit	
H+	0.00	H2	0.00	H2	0.00
He+	-1.02	He	-0.71	He	-0.71
O++	-3.52	H2O	-3.43	H2O#	-3.43
C++	-3.86	CO	-3.63	CO	-3.63
N++	-4.10	Ne	-3.74	Ne	-3.74
S++	-6.73	NH3	-3.81	NH3#	-3.81
Si++	-7.76	C2H4	-4.68	C2H4#	-4.68
Mg++	-7.97	NH2	-5.32	NH2#	-5.32
Na++	-8.64	O	-5.61	O	-5.61
Fe++	-8.76	Ar	-5.61	Ar	-5.61

* Abundances are expressed as the $\log_{10}$ of the abundance relative to the most abundant species.

Appendix C: Freeze-out of elements

While several of the ices appear at the CPD midplane only as trace species (e.g. SO_2) the freeze-out of the corresponding elements may be complete. The fraction of carbon, oxygen, nitrogen, and sulfur nuclei which are found as ice at each radius in the CPD midplane at t_{visc} = 10^4 yr for the reset, partial reset, and inheritance cases can be found in Fig. C.1. In all cases Sulfur is found to have frozen-out of the gas almost entirely where possible. This is consistent with the origin of Io's sulfur being in the form of refractory iron sulfides, rather than as e.g. SO_2#, as we find it co-deposited with H_2O# in all cases (Carlson et al. 2007).

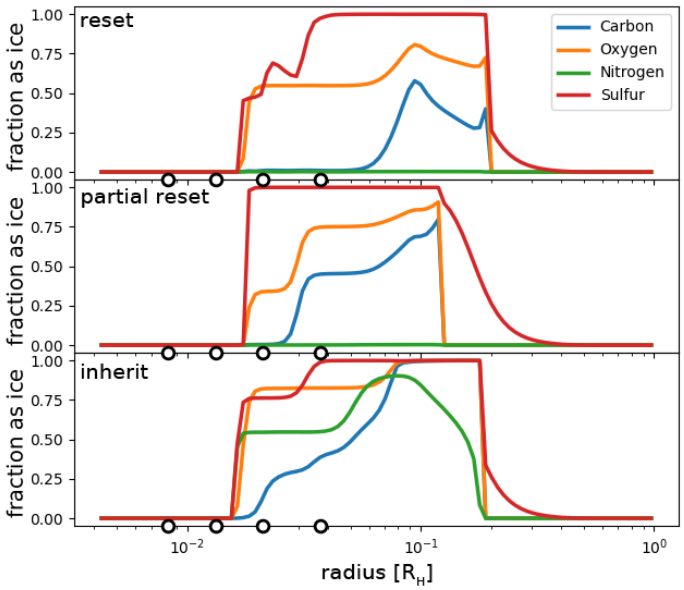

Fig. C.1: The fraction of nuclei of various elements which are found in the ice at the midplane of the CPD for the three initial conditions. Properties have been extracted from the low viscosity CPD with the viscous timescale of 10^4 yr. Radius is in units of the Jupiter Hill radius. The four empty circles indicate the position of the Galilean satellites.